Optical conductivity of the metallic pyrochlore iridate Pr2Ir2O7: influence of spin-orbit coupling and electronic correlations on the electronic structure

Harish Kumar, Matthias Köpf, P. Telang, N. Bura, Anton Jesche, Philipp Gegenwart, Christine A. Kuntscher

Angaben zur Veröffentlichung / Publication details:

Kumar, Harish, Matthias Köpf, P. Telang, N. Bura, Anton Jesche, Philipp Gegenwart, and Christine A. Kuntscher. 2024. "Optical conductivity of the metallic pyrochlore iridate Pr2Ir2O7: influence of spin-orbit coupling and electronic correlations on the electronic structure." *Physical Review B* 110 (3): 035140. https://doi.org/10.1103/physrevb.110.035140.

Optical conductivity of the metallic pyrochlore iridate $Pr_2Ir_2O_7$: Influence of spin-orbit coupling and electronic correlations on the electronic structure

Harish Kumar,[1,*] M. Köpf,[1] P. Telang,[2] N. Bura,[1] A. Jesche,[2] P. Gegenwart,[2] and C. A. Kuntscher[1,†]
[1]*Experimental Physics II, Institute of Physics, University of Augsburg, 86159 Augsburg, Germany*
[2]*Experimental Physics VI, Center for Electronic Correlations and Magnetism, University of Augsburg, 86159 Augsburg, Germany*

(Received 7 May 2024; revised 19 June 2024; accepted 25 June 2024; published 15 July 2024)

The synergy of strong spin-orbit coupling and electron-electron interactions gives rise to unconventional topological states, such as topological Mott insulator, Weyl semimetal, and quantum spin liquid. In this study, we have grown single crystals of the pyrochlore iridate $Pr_2Ir_2O_7$ and explored its magnetic, lattice dynamical, and electronic properties. While Raman spectroscopy data reveal six phonon modes confirming the cubic $Fd\bar{3}m$ crystal symmetry, dc magnetic susceptibility data show no anomalies and hence indicate the absence of magnetic phase transitions down to 2 K. Both temperature-dependent electric transport and optical conductivity data reveal the metallic character of $Pr_2Ir_2O_7$. The optical conductivity spectrum contains a midinfrared absorption band, which becomes more pronounced with decreasing temperature due to spectral weight transfer from high to low energies. The presence of the midinfrared band hints at the importance of correlation physics. The optical response furthermore suggests that $Pr_2Ir_2O_7$ is close to the Weyl semimetal phase.

DOI: 10.1103/PhysRevB.110.035140

I. INTRODUCTION

Pyrochlore iridates $A_2Ir_2O_7$, with A = Y, Bi and rare earths R, have garnered significant interest due to their distinctive properties, such as frustration, the presence of iridium, and the potential for novel topological phases [1,2]. The substantial spin-orbit coupling (SOC) arising from iridium's heavy nature, coupled with the extended $5d$ orbitals minimizing electronic correlation (U) effects, contributes to the intriguing nature of these materials. In iridates, SOC, U, and crystal electric field effect (CEF) exhibit comparable strength, and balancing these energies can lead to the emergence of distinct topological phases [1–3]. The CEF induces the splitting of $5d$ orbitals into t_{2g} and e_g states, and the robust SOC divides the t_{2g} level into a $J_{\text{eff}} = 1/2$ doublet and a $J_{\text{eff}} = 3/2$ quartet. In the pyrochlore iridates, the Ir has a 4+ valency with a $5d^5$ configuration, resulting in a spin-orbital moment $J_{\text{eff}} = 1/2$ scenario. The small U leads to the $J_{\text{eff}} = 1/2$ splitting into a lower and an upper Hubbard band, introducing interesting physics, related to the spin-orbit Mott insulator (MI) state. Recent theoretical investigations proposed intriguing topological states for pyrochlore iridates [1–4]. Initially, Wan *et al.* introduced a Weyl semimetal (WSM) phase for the magnetic pyrochlores, featuring an all-in/all-out antiferromagnetic (AFM) order that preserves structural symmetry while breaking time-reversal symmetry [3]. Depending on the strength of U, either an MI with an all-in/all-out magnetic structure or a WSM phase with 24 Weyl nodes at the Fermi surface was predicted [3].

R-pyrochlore iridates containing $5d$ electrons (Ir^{4+}) generally demonstrate an insulating AFM state, where this behavior is typically suppressed with an increase in the size of the R-ion [5–9]. Accordingly, $Pr_2Ir_2O_7$ is not insulating, but displays a paramagnetic (PM) metallic nature [6,8,10]. This is further confirmed by optical studies, where systems containing Y, Dy, Eu, and Sm demonstrate a distinct optical gap ($\Delta_g > 0.2$ eV) that diminishes with larger A-cations, as evidenced by Nd and Pr materials [11,12]. Namely, $Nd_2Ir_2O_7$ contains unconventional free charge, evidenced by the quadratic temperature dependence of the Drude spectral weight, which is consistent with the characteristics expected for massless Dirac electrons. However, it is notable that the entropy counterpart does not exhibit a T^3 contribution in the specific heat [13]. Moreover, the substituted material $Nd_2(Ir_{1-x}Rh_x)_2O_7$ demonstrates a transition from a narrow-gap MI to a WSM and ultimately to a correlated metal as x increases [12]. In addition, the optical response of $Eu_2Ir_2O_7$ exhibits a linear-in-frequency behavior at low temperatures, suggesting the characteristic signature of the WSM phase [14]. In other pyrochlore iridates, infrared (IR) studies of $Bi_2Ir_2O_7$ and $Pb_2Ir_2O_7$ show a strongly metallic ground state and a sizable mid-IR absorption band at around 0.2 eV and 0.4 eV, respectively [15,16]. The presence of an AFM state in most pyrochlore iridates breaks time-reversal symmetry while preserving crystal symmetries; however, $Pr_2Ir_2O_7$ is an exceptional case among the R pyrochlores [2,6,8].

For $Pr_2Ir_2O_7$, theoretical predictions propose a quadratic band touching at the zone center [17], which has been confirmed by angle-resolved photoemission spectroscopy experiments [18]. The presence of a magnetic and sizable Pr^{3+} ($4f^2$) ion adds to its distinctive nature. $Pr_2Ir_2O_7$ consists of two magnetically active sublattices, Pr and Ir, forming corner-shared tetrahedra (Fig. 1) and introducing magnetic frustration. Interestingly, an AFM Ruderman-Kittel-Kasuya-Yosida (RKKY) interaction with an energy scale of $T_N \sim 20$ K between Pr-$4f$ moments, mediated through Ir-$5d$

*Contact author: harish.kumar@physik.uni-augsburg.de
†Contact author: christine.kuntscher@physik.uni-augsburg.de

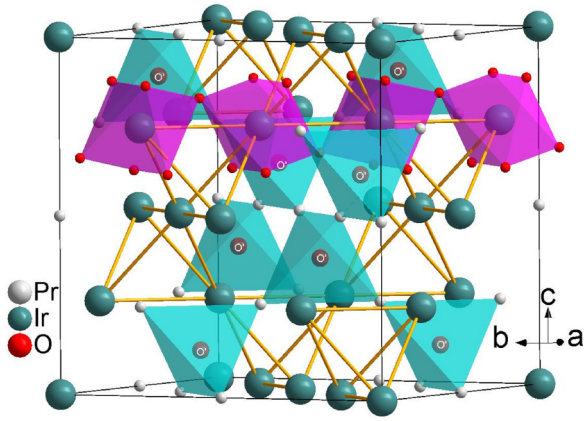

FIG. 1. The cubic pyrochlore structure shows corner-shared tetrahedral arrangements of Pr_4O' (in cyan) and $Ir_4\diamond$ (in orange edges), where $\diamond$ represents empty center-site (8a-site) [7]. Additionally, the structure includes IrO_6 octahedra (in light magenta).

delocalized electrons, has been observed [6]. The AFM interaction experiences a suppression due to the screening of $4f$ moments through the Kondo effect, resulting in a reduction of the Weiss temperature to $\theta_{CW} = 1.7$ K. Notably, below 1.7 K, the susceptibility of $Pr_2Ir_2O_7$ exhibits an $\ln T$ dependence [6] and thermodynamic measurements indicate a quantum critical scaling, interpreted as a signature for a metallic spin liquid phase [19].

Additionally, an unusual anomalous Hall effect (AHE) has been identified below 1 K in $Pr_2Ir_2O_7$ which is elucidated by the spin-chirality effect in Ir-5d electrons, arising from the noncoplanar spin structure of Pr spins [20]. The noteworthy observation of AHE, even in the absence of uniform magnetization at zero field, provides compelling evidence for the existence of the long-sought chiral spin liquid state in $Pr_2Ir_2O_7$ [21]. More intriguingly, from a theoretical perspective, this material is proposed to be situated in proximity to an interaction-driven AFM quantum critical point (QCP) [22] compatible with the experimental signatures [19]. This QCP has been considered as a pivotal transition point between an AFM WSM and a nodal non-Fermi liquid phase [22]. Furthermore, Ueda *et al.* identified distinct signatures of topological transitions within the WSM states for $Pr_2Ir_2O_7$ under the influence of a magnetic field, prominently attributed to the $f - d$ coupling [23].

In this work, we present the synthesis of $Pr_2Ir_2O_7$ single crystals and their comprehensive characterization. In Secs. A, B, and C, we present the magnetic and charge transport properties, as well as Raman spectroscopy results, which align with previous findings. However, our main focus lies in investigating the optical properties of $Pr_2Ir_2O_7$. The optical conductivity spectrum contains a Drude contribution revealing the metallic character of $Pr_2Ir_2O_7$ and high-energy excitations due to transitions between $J_{\text{eff}} = 3/2$ and $J_{\text{eff}} = 1/2$ bands. Furthermore, an absorption band in the mid-IR frequency range whose spectral weight is growing with decreasing temperature suggests the importance of electronic correlations. The results are compared with recent findings for closely related metallic pyrochlore iridates and discussed in terms of correlated semimetals.

II. EXPERIMENTAL DETAILS

Single crystals of $Pr_2Ir_2O_7$ were grown using polycrystalline material synthesized via the potassium fluoride (KF) flux method within a platinum crucible. The polycrystalline precursor was prepared by combining Pr_6O_{11} and Ir powders in a stoichiometric ratio, each with a phase purity exceeding 99.99% (M/s Sigma-Aldrich). The Pr_6O_{11} underwent a preheat treatment at 800°C for ∼8 hours to eliminate residual atmospheric moisture. The thoroughly ground mixture of Pr_6O_{11}, and Ir, further mixed with ∼2% KF by the mixture's mass, was further ground to obtain a homogeneous composition. This well-mixed powder was then pelletized and sintered in air at a temperature of 800°C for 48 hours, involving an intermediate grinding step to enhance the material's homogeneity and crystalline structure. The phase purity of the material was checked with powder x-ray diffraction (XRD) using a Rigaku diffractometer with CuK_α radiation.

To synthesize the single crystals, the obtained polycrystalline $Pr_2Ir_2O_7$ material is blended with KF flux and the excess of IrO_2, and subjected to calcination in a platinum crucible, and comprehensive details of crystal growth are provided in Refs. [24,25]. Within the Pt-crucible, a collection of octahedron-shaped crystals emerges at the bottom. Subsequently, the crystals are carefully extracted from the crucible using distilled hot water, revealing a characteristic size of approximately ∼1 mm, as illustrated in Fig. 2(a). The chemical composition of the $Pr_2Ir_2O_7$ crystals was verified using energy dispersive analysis of x-ray (EDX) on a ZEISS Crossbeam 550/550L scanning electron microscope, equipped with an Oxford detector. The obtained atomic percentages of Pr and Ir in $Pr_2Ir_2O_7$ are 19.8% and 19.4%, respectively. Previous studies have shown that stoichiometry significantly impacts the electronic properties of $R_2Ir_2O_7$, as confirmed by the ratio of Pr and Ir [26]. In $Pr_2Ir_2O_7$, the ratio of Pr and Ir is found to be 1.02, which closely aligns with the nominal concentration. Raman spectroscopy measurements were performed on $Pr_2Ir_2O_7$ single crystals utilizing a confocal micro-Raman setup featuring a Jobin-Yvon T64000 spectrograph and a 488 nm argon ion laser as an excitation source was employed.

Temperature- and field-dependent magnetization data have been collected using a SQUID magnetometer (MPMS). Electrical transport properties have been investigated in the temperature range of 2–300 K using a four-probe technique with PPMS from Quantum Design. Temperature-dependent IR spectroscopy measurements were conducted with unpolarized electromagnetic radiation in the frequency range of 210–18,000 cm^{-1} (26 meV to 2.23 eV) within a temperature range of 300 K to 5 K. This was done using a CryoVac Konti cryostat connected to a Bruker Vertex 80v FTIR spectrometer, coupled with a Bruker Hyperion IR microscope. For reflectivity measurements, the (111) crystal surface was polished with diamond paper. To obtain absolute reflectivity, a silver layer was deposited onto half of the polished crystal surface, serving as reference [27,28]. Subsequently, the sample was fixed to a sample holder within the cryostat using low-temperature GE varnish, ensuring its alignment

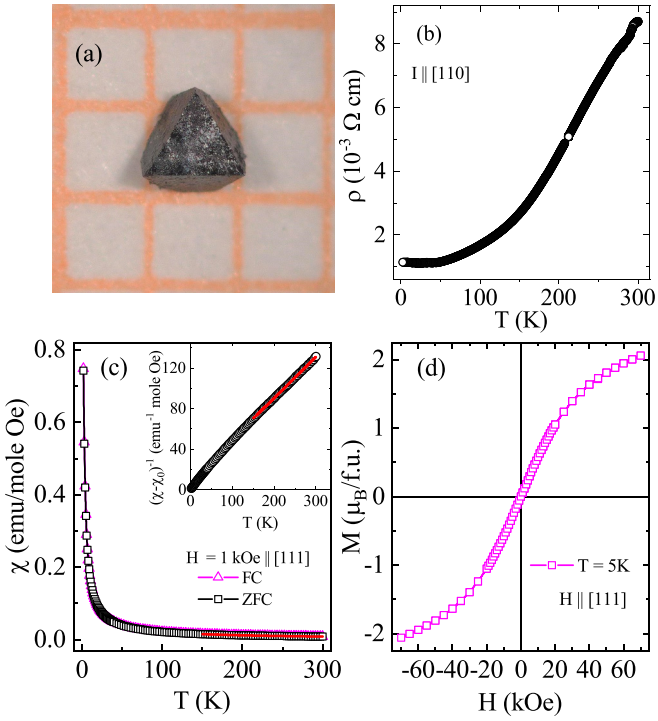

FIG. 2. (a) Image of a $Pr_2Ir_2O_7$ single crystal. (b) The dc electrical resistivity $\rho(T)$ data of $Pr_2Ir_2O_7$ as a function of temperature. (c) Temperature-dependent magnetic susceptibility data of $Pr_2Ir_2O_7$, where the solid line in the high-temperature regime is fit to Eq. (1). The inset of (c) shows the inverse magnetic susceptibility $(\chi - \chi_0)^{-1}(T)$ data with a straight-line fitting in the high-temperature regime. (d) Magnetic field–dependent magnetization of $Pr_2Ir_2O_7$ measured at 5 K.

perpendicular to the incident beam. In the far-IR range, the frequency resolution was set to 1 cm^{-1}, whereas a resolution of 4 cm^{-1} was selected for the higher-frequency range. The obtained reflectivity spectrum was extrapolated in the low- and high-energy regimes using Drude-Lorentz fitting and x-ray optic volumetric data, respectively [29]. It is important to note that a power-law (ω^n) interpolation with an integer $n = 3$ was applied to bridge the region between measured reflectivity and calculated high-energy extrapolated data. From the resulting reflectivity spectrum, the real part of the optical conductivity $\sigma_1(\omega)$ was calculated through Kramers-Kronig relations. Further, the Drude-Lorentz model was adeptly applied for fitting the optical spectra, facilitated by the RefFIT program [30].

III. RESULTS

A. Magnetic properties

Figure 2(c) depicts the temperature-dependent magnetization $M(T)$ data for $Pr_2Ir_2O_7$, recorded from 2 to 300 K under an applied fields H = 1 kOe along the (111) direction following zero-field-cooled (ZFC) and field-cooled (FC) protocol. The magnetic moment increases as temperature decreases, with a notable increase below around 30 K, consistent with prior studies [6,8,10]. The absence of magnetic irreversibility between ZFC and FC magnetization suggests a PM behavior for this material. A representative fit of the $\chi(T)$ data with modified Curie-Weiss behavior [Eq. (1)] in the temperature range of 150–300 K is presented in Fig. 2(c) as a solid line [6,8,31].

$$\chi(T) = \chi_0 + \frac{C}{(T - \theta_{CW})} \quad , \tag{1}$$

where the variables χ_0, C, and θ_{CW} represent the temperature-independent magnetic susceptibility, Curie constant, and Curie-Weiss temperature, respectively. The reasonably good fit with Eq. (1) indicates that the magnetic state in the PM state obeys modified Curie-Weiss behavior. The fitting yields a Curie temperature $\theta_{CW} = -23$ K, consistent with prior studies [6,8]. The corrected inverse susceptibility $(\chi - \chi_0)^{-1}$ versus T exhibits a linear behavior in the high-temperature regime [see the inset of Fig. 2(c)].

Remarkably, the emergence of a finite θ_{CW} for $Pr_2Ir_2O_7$, in the absence of a Neel temperature (T_N), is important to note. This finite $|\theta_{CW}|$ occurs due to Ir-5d electron-mediated AFM-type RKKY interactions among Pr-4f atoms [6]. This observation finds further support in recent experiments involving the substitution of magnetic Pr at the nonmagnetic Y-site in $(Y_{1-x}Pr_x)_2Ir_2O_7$, where the magnitude of θ_{CW} rapidly weakens with increasing Pr content [8]. It is believed that this reduction in $|\theta_{CW}|$ is attributed to the $f - d$ interaction between localized Pr-4f and itinerant Ir-5d electrons. Using the value of the Curie constant $C = 2.4$, we have calculated the effective magnetic moment μ_{eff} according to $\mu_{eff} = \sqrt{3k_BC/(N_A\mu_B^2)} = 2.83\sqrt{C}$. The so-obtained value of $\mu_{eff} = 4.38\ \mu_B$/f.u. is quite close to the reported results [6,8].

The magnetic field dependence data $M(H)$ measured at 5 K in the field range of ± 70 kOe applied along (111) is depicted in Fig. 2(d). As is evident in the figure, the magnetic moment exhibits a nonlinear increase with increasing field, with no signs of saturation observed up to 70 kOe. The moment recorded at 5 K under the highest measuring field (70 kOe) is approximately 2.05 μ_B/f.u., consistent with previously reported values [8,32].

B. Electric transport

To comprehend the electronic conduction characteristics of $Pr_2Ir_2O_7$, we performed dc resistivity $\rho(T)$ measurements as a function of temperature in a four-probe geometry. As is evident in Fig. 2(b), $\rho(T)$ monotonically decreases with decreasing temperature down to ~45 K evidencing metallic behavior. Between ~45 K and 25 K, $\rho(T)$ changes only slightly, followed by a subtle increase below 25 K down to 2 K. The decrease in resistivity with lowering the temperature with a minimum at around 25 K is consistent with previous studies [6,8,10,33] and it follows a logarithm ($\ln T$) dependence (not shown), indicative of the Kondo effect in $Pr_2Ir_2O_7$ arising due to $f - d$ interaction between localized Pr-4f magnetic ions and itinerant Ir-5d electrons [6,8].

C. Raman spectroscopy

To confirm the cubic $Fd\bar{3}m$ symmetry of $Pr_2Ir_2O_7$, Raman spectroscopy has been employed. Room-temperature Raman spectroscopy data of $Pr_2Ir_2O_7$ are depicted in Fig. 3.

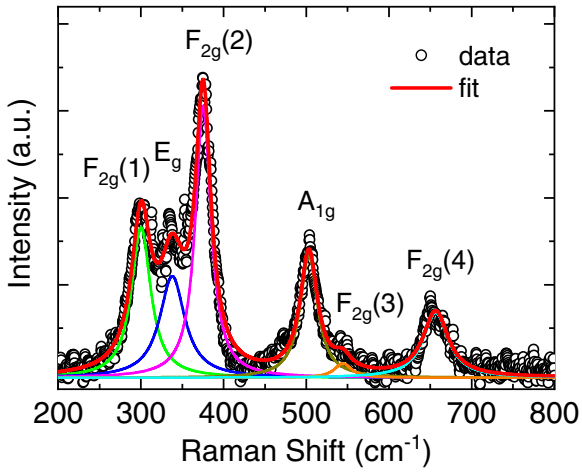

FIG. 3. Raman spectrum for $Pr_2Ir_2O_7$ at room temperature together with the total fit and the individual phonon mode contributions.

According to the cubic phase with $Fd\bar{3}m$ symmetry, six Raman active modes are expected based on the factor group analysis [34,35]:

$$\Gamma_{\text{optic}} = [A_{1g} + E_g + 4F_{2g}]_R + [7T_{1u}]_{IR}, \quad (2)$$

where R and IR indicate the Raman and IR active modes, respectively. In Fig. 3, six distinctive Raman modes of $Pr_2Ir_2O_7$ are observed and tabulated in Table I. The spectrum characteristics and the position of the modes confirm the cubic $Fd\bar{3}m$ symmetry and align seamlessly with prior theoretical and experimental studies, as indicated in Refs. [34–36].

D. IR spectroscopy

To comprehend the evolution of the electronic band structure, we conducted reflectivity measurements on the (111) crystal surface covering a broad frequency range. Figure 4(a) shows the temperature-dependent reflectivity spectrum for various temperatures. From the room-temperature reflectivity spectrum $R(\omega)$, we identified four IR-active phonon modes in the measured far-IR region and list them in Table I. The L_1, L_2, L_3, and L_4 IR modes are associated with the motion of the Ir—O—Ir bond. Specifically, L_1 corresponds to bending (out-of-plane) mode, whereas L_2 and L_3 correspond to bending (in-plane) modes, and L_4 is related to the stretching mode [37]. The positions of the observed IR modes are consistent with both theoretical and experimental values [34]. $R(\omega)$ intriguingly rises with decreasing temperature in the mid- and far-IR regime, displaying a heightened level in the far-IR region at 5 K and approaches unity at the lowest frequencies, indicating the metallic nature for $Pr_2Ir_2O_7$. The temperature-dependent $R(\omega)$ spectra of $Pr_2Ir_2O_7$ exhibit a notable hump or plasma edge-type characteristic around the mid-IR region (∼0.15 eV), followed by a gradual reduction in reflectivity as the frequency extends up to 2 eV.

TABLE I. Raman modes at 300 K and T_{1u} IR-active modes (labeled $L_1 \ldots L_4$) observed at 300 and 5 K.

Raman Modes (cm^{-1})						
T(K)	F^1_{2g}	E_g	F^2_{2g}	A_{1g}	F^3_{2g}	F^4_{2g}
300 K	300.2	338.0	375.4	503.2	544.3	656.4
IR Modes (cm^{-1})						
T(K)	L_1	L_2	L_3	L_4		
300 K	338.1	408.4	463.5	575.7		
5 K	350.4	407.7	451.3	579.8		

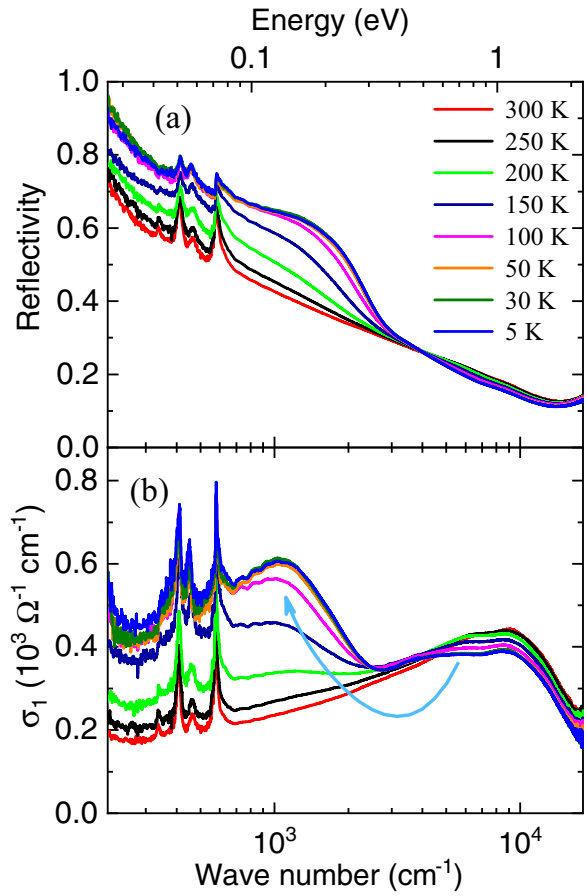

FIG. 4. (a) Reflectivity and (b) optical conductivity σ_1 spectra of $Pr_2Ir_2O_7$ as a function of temperature. The curved arrow in (b) highlights the spectral weight transfer from high to low frequencies with cooling.

The corresponding optical conductivity spectra $\sigma_1(\omega)$, which were derived from the reflectivity spectra through Kramers-Kronig analysis, are depicted in Fig. 4(b). The total spectral weight is conserved in the frequency range 0–18 000 cm^{-1} for all measured temperatures. At room temperature, the $\sigma_1(\omega)$ spectra display a Drude term at low frequencies due to intraband transitions, suggesting the metallic nature of $Pr_2Ir_2O_7$. Additionally, four IR modes are observed in the far-IR region, and a mid-IR absorption peak, along with four interband features, is observed in the high-frequency region (to be discussed later). Analysis of temperature-dependent $\sigma_1(\omega)$ spectra reveals several key observations. First, the optical conductivity undergoes marked changes with temperature. A clear rise in conductivity is evident in the far-IR region with decreasing temperature, consistent with the metallic nature of

$Pr_2Ir_2O_7$. Notably, the magnitude of optical conductivity at the lowest measured frequencies is consistent with the measured dc conductivity using the four-probe method (discussed later). Second, the most noticeable change in the optical conductivity occurs in the low-energy part (mid-IR region) of the spectrum, which is composed of a broad and prominent M-band at ∼0.12 eV [see Fig. 4(b)], and it becomes more prominent with lowering the temperature. Third, there is a spectral weight (SW) transfer from the high-energy side to the low-energy side (mid-IR) with lowering the temperature, as indicated by the curved arrow in Fig. 4(b), passing through an isosbestic point at around ∼4000 cm^{-1}. A similar type of spectral weight transformation has been seen in $A_2Ir_2O_7$ when transitioning from insulating (Y, Dy, Eu) to metallic (Nd, Pr) phases [11].

For quantitative analysis, we employed the Drude-Lorentz model to reproduce the $\sigma_1(\omega)$ spectrum, where the Drude component describes the free charge carrier excitations and the Lorentz terms are associated with phonon excitations and interband transitions. The general formula for the Drude-Lorentz model is expressed as follows [38]:

$$\sigma_1(\omega) = \frac{\omega_p^2}{4\pi}\frac{\tau_D}{1+\omega^2\tau_D^2} + \sum_j \frac{S_j}{4\pi}\frac{\omega^2/\tau_j}{\left(\omega_j^2-\omega^2\right)^2+\omega^2/\tau_j^2}, \quad (3)$$

where the first term represents the Drude contribution and the latter terms the Lorentz-type excitations. Within the Drude term, the ω_p and $1/\tau_D$ denote the plasma frequency and relaxation rate of individual conduction bands. The scattering rate γ_D of the Drude peak can be derived from the relaxation rate using $\gamma_D = 1/(2\pi c\tau_D)$, where c represents the speed of light. Meanwhile, the plasma frequency is defined as $\omega_P^2 = 4\pi ne^2/m^*$, where n is the carrier concentration and m^* is the effective mass of the charge carriers. In the second term, ω_j, $1/\tau_j$, and S_j are the resonance frequency, broadening of the oscillator (width $= 1/2\pi c\tau_j$), and mode strength for the jth Lorentz oscillator, respectively. An essential aspect of conductivity is its spectral weight $SW = \int \sigma_1(\omega)d\omega$, defined as the integral of the optical conductivity over specific frequency intervals. Integrating $\sigma_1(\omega)$ over finite frequency ranges, particularly where distinct features such as interband excitations are observed, quantifies the number of electrons involved in particular features like interband excitation processes. For the Drude term, the SW_D is related to the plasma frequency according to $\omega_p^2/8$ [38] and will be discussed later (see Fig. 7).

Considering the metallic nature of $Pr_2Ir_2O_7$, we incorporated one Drude term (D) for excitations of itinerant carriers, along with five Lorentz oscillators labeled M, A, B, B', and C corresponding to electronic transitions. Hall transport investigations revealed that $Pr_2Ir_2O_7$ predominantly exhibits electron-type charge carriers, characterized by a carrier concentration of $n = 4.13 \times 10^{21}$ cm^{-3} [20]. Consequently, a single Drude term is employed to characterize the optical conductivity. Figures 5(a) and 5(b) illustrate the optical conductivity of $Pr_2Ir_2O_7$ in the entire measured frequency range, showing representative Drude-Lorentz fits and individual fit contributions at 5 K and 300 K, respectively. The observed IR modes at 5 and 300 K for $Pr_2Ir_2O_7$ are depicted in Fig. 5 by using L_1, L_2, L_3, and L_4 notations and are tabulated in Table I.

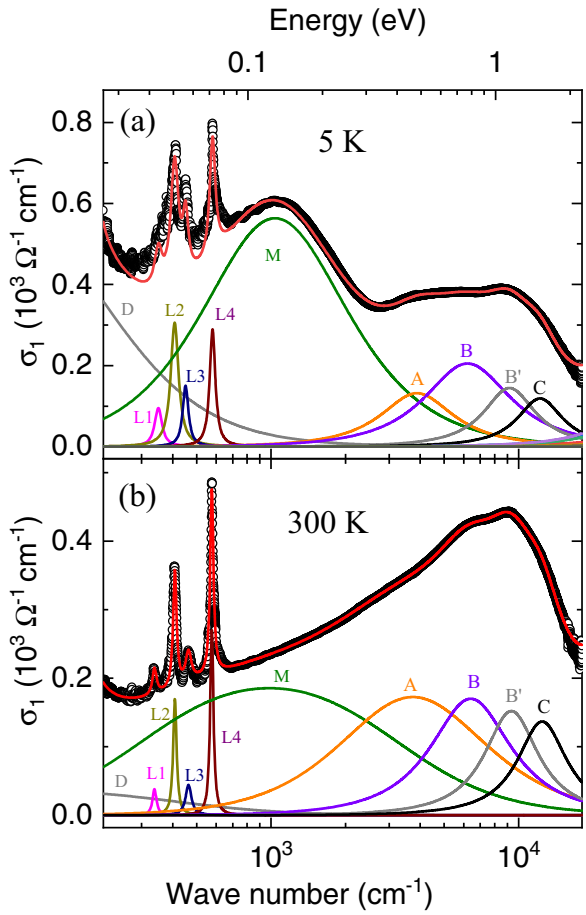

FIG. 5. Optical conductivity σ_1 spectrum at (a) 5 K and (b) 300 K together with the Drude-Lorentz fit and the fit contributions.

In the high-energy $\sigma_1(\omega)$ spectrum, four distinct Lorentz contributions are identified at ∼0.46 eV (A), ∼0.79 eV (B), ∼1.15 eV (B'), and ∼1.54 eV (C). Consistent with other iridates [28,39,40], the last three excitations (B, B', and C) are associated with transitions between $J_{\text{eff}} = 3/2$ and $J_{\text{eff}} = 1/2$ states, exhibiting potential additional splittings due to octahedral distortion [28], as illustrated in the energy band scheme depicted in Fig. 6. The observed peak A around ∼0.46 eV closely aligns with reported values for iridates [28,39,41,42]. This spectral feature predominantly arises from transitions within the $J_{\text{eff}} = 1/2$ band split by electron correlations. It is noteworthy that with decreasing temperature, these excitations experience a slight shift (approximately 0.02 eV) toward the low-energy side, except the A peak, which shifts to higher energy by a similar amount. We highlight the pivotal role of strong SOC, which prevents the merging of these interband features into a single transition from t_{2g} to e_g bands. Consequently, we deduce that SOC plays a pivotal role in shaping the electronic structure of $Pr_2Ir_2O_7$.

Besides these excitations, the M-band and the Drude contribution (D) exhibit interesting changes with temperature. Figures 7(a)–7(d) show the temperature-dependent mode strength of the M-band (S_M), spectral weight of Drude (SW_D), scattering rate of Drude (γ_D), and dc conductivity data (σ_{dc}) obtained from the four-probe method and optical $\sigma_1(\omega)$ data,

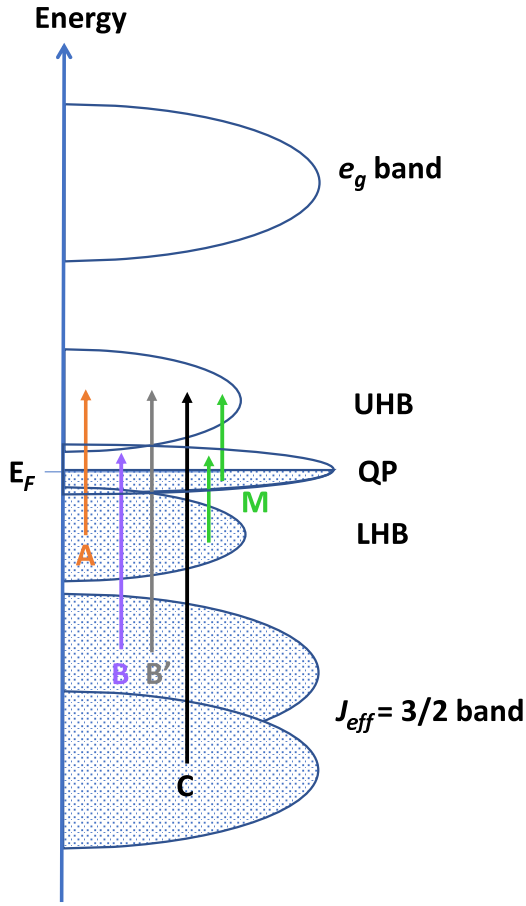

FIG. 6. Suggested energy band scheme of $Pr_2Ir_2O_7$ based on its optical conductivity. The labeled arrows B, B', and C correspond to transitions from $J_{\text{eff},3/2}$ to $J_{\text{eff},1/2}$, whereas A is attributed to excitations between the Hubbard bands. Additionally, the M denotes transitions either from the lower Hubbard band to the QP peak or from the QP peak to the upper Hubbard band.

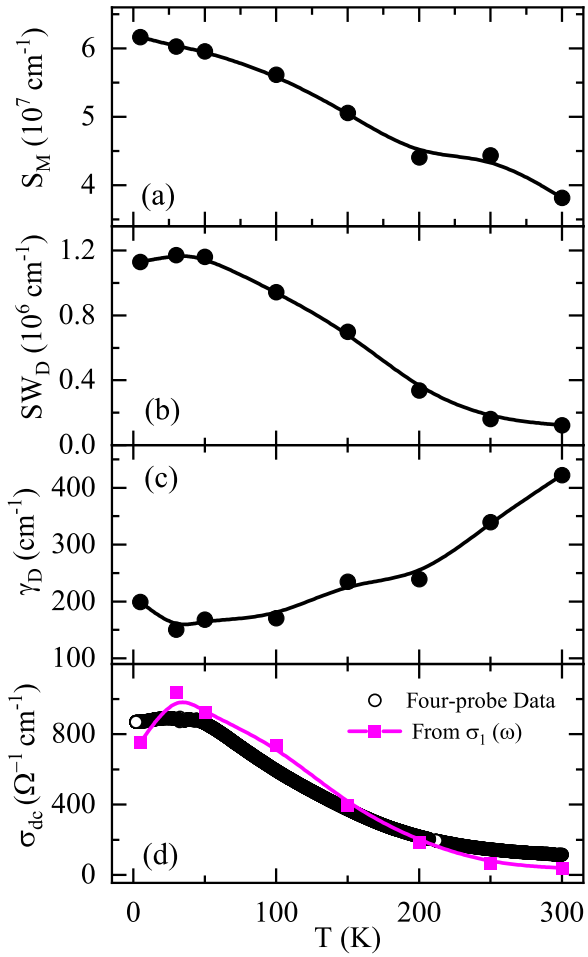

FIG. 7. (a) Mode strength S_M of the M-band, (b) spectral weight SW_D of the Drude term, (c) scattering rate γ_D of the Drude term, and (d) dc conductivity σ_{dc} obtained from a four-probe method and extracted from $\sigma_1(\omega)$ data, respectively, as a function of temperature.

respectively. The strength S_M of the M-band and the spectral weight of the Drude term SW_D both increase with lowering the temperature [see Figs. 7(a) and 7(b), respectively]. The scattering rate γ_D of the itinerant charge carriers decrease with decreasing temperature [see Figs. 7(c)] and amounts to 200 cm^{-1} at 5 K. This value yields a scattering time τ of about 2.6×10^{-14} seconds, derived from the formula $\gamma_D = 1/(2\pi c\tau)$. Employing the obtained τ value, the carrier mobility μ is calculated using the expression $\mu = e\tau/m^*$, where m^* is the effective carrier mass. A recent photoemission study of $Pr_2Ir_2O_7$ has revealed an effective carrier mass (m^*) of 6.3 times the mass of a free electron (m_0) [18]. Subsequently, the resulting mobility is estimated at around 7.4 cm^2/Vs, a value in close agreement with the reported electrical transport mobilities in single crystals (~4.19 cm^2/Vs) [6,20] and thin films (~12 cm^2/Vs) [43].

It is important to note that both mode strength of the M-band and spectral weight of the Drude term (D) increase with lowering the temperature. The M-band in the mid-IR range has been analyzed within the context of the quasiparticle (QP) peak approach in metallic systems. It primarily arises from transitions between the coherent QP peak at the Fermi energy and the Hubbard bands (discussed later) [44]. Furthermore, we note that the dc conductivity as a function of temperature, as extracted from the optical conductivity data, fully agrees with the electric transport results presented earlier [see Fig. 7(d)]. It is important to note that the Kondo effect is revealed in the temperature-dependent σ_{dc} data as a broad maximum at around 30 K. Hence, the decrease in the Drude spectral weight SW_D and the increase in the carrier scattering rate below ~30 K might be related to the Kondo effect or the AHE [6,8,20].

IV. DISCUSSION

According to our prior discussion, $Pr_2Ir_2O_7$ is an interesting material in the context of exotic topological states in pyrochlore iridates [1–6]. As illustrated in Figs. 4 and 5, the optical conductivity within the low-energy regime (mid-IR range) exhibits a pronounced temperature dependence throughout the studied temperature range. The significance of novel topological phases such as three-dimensional (3D) Weyl/Dirac materials and quadratic band touching is important in the current context [11,14,15,17,18]. Generally,

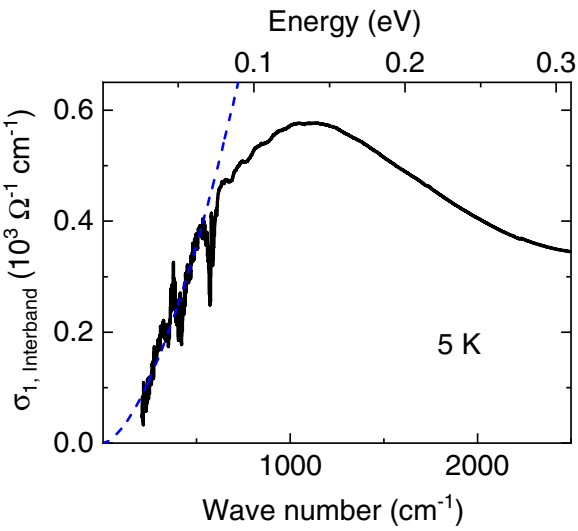

FIG. 8. Interband optical conductivity $\sigma_{1,\mathrm{interband}}$ at 5 K obtained by subtracting the Drude term (D) and the phonon mode contributions from the total σ_1 spectrum. The dashed line indicates a fit with a power law behavior as described in the text.

the interband optical conductivity in d dimension obeys the universal formula $\sigma_1 \propto \omega^{(d-2)/z}$, where z represents the exponent in the band dispersion relation $E(k) \propto |k|^z$ [45]. In 3D ($d = 3$) materials characterized by parabolic band dispersion ($z = 2$), σ_1 follows a square root frequency dependence according to $\sigma_1 \propto \omega^{0.5}$ [46]. Furthermore, the observed linear-in-frequency behavior of the interband optical conductivity in a 3D system serves as a distinct indication of linear band dispersion ($z = 1$), a characteristic feature of WSM/Dirac materials [47]. A recent study of $Nd_2Ir_2O_7$ shows that the $\sigma_1(\omega)$ exhibits a linear-in-frequency (ω) dependence in the low-energy region [13]. Additionally, there is a notable transfer of spectral weight from the Drude to the interband component of $\sigma_1(\omega)$ as temperature decreases and the Drude spectral weight exhibits a T^2 dependence [13,48]. Furthermore, the application of an external magnetic field can modulate the valley population in the Weyl phase through $f - d$ coupling [49].

First, we note that we do not observe a T^2 dependence in the Drude spectral weight SW_D [see Fig. 7(b)]. To further check the preceding point, we subtract the Drude term (D) and the phonon modes contributions from the total $\sigma_1(\omega)$ spectrum of 5 K data. The so-obtained interband conductivity $\sigma_{1,\mathrm{Interband}}(\omega)$ is depicted in Fig. 8. The spectral shape of the present $\sigma_{1,\mathrm{Interband}}(\omega)$ data does neither conform to the characteristic behavior of 3D quadratic band touching [13,50], $\sigma_{1,\mathrm{Interband}}(\omega) \propto \omega^{0.5}$, nor to the expected frequency dependence of 3D Weyl/Dirac cones [11,13,45,47], $\sigma_{1,\mathrm{Interband}}(\omega) \propto \omega$. We also tried the power law behavior $\sigma_{1,\mathrm{Interband}}(\omega) \propto \omega^n$ (where n is the exponent) for the lowest measured 5 K $\sigma_{1,\mathrm{Interband}}(\omega)$ spectra, as depicted in Fig. 8. The fit yields an exponent $n = 1.62(1)$, which closely aligns with the observed value for $Nd_2Ir_2O_7$ where it signals the emergence of the correlation-gapped WSM phase [13]. Intriguingly, in contrast to $Nd_2Ir_2O_7$ which undergoes a metal-to-insulator transition (MIT) and magnetic ordering at $T_N \sim 33$ K [5], $Pr_2Ir_2O_7$ maintains a PM metallic nature [6,8]. The observed exponent n suggests that $Pr_2Ir_2O_7$ is in proximity to the WSM phase. $Pr_2Ir_2O_7$ is conjectured to reside near an AFM QCP [19,22]. This QCP has been extensively explored as a crucial transition boundary between an AFM WSM and a phase characterized by a nodal non-Fermi liquid [22]. Additionally, Ueda *et. al* found the signatures of topological transitions among the WSM states for $Pr_2Ir_2O_7$ under the influence of a magnetic field, arising notably from the $f - d$ coupling [23]. Hence, the observed value of n for $Pr_2Ir_2O_7$ implies the proximity of the WSM phase. This observation underscores the need for more comprehensive investigations to potentially transition the current material toward the WSM side through dedicated perturbation of the Pr-site with a smaller A-ionic size or by applying external pressure.

Next, we discuss the relevance of electronic correlations for the interpretation of the optical conductivity of $Pr_2Ir_2O_7$. In many correlated materials, spectral weight due to intraband excitations, primarily located in the far-IR range, is significantly suppressed and transferred to higher frequencies in the mid- and near-IR [15]. The existence of the M-band in the optical conductivity of $Pr_2Ir_2O_7$ may thus be attributed to electron correlation effects. The strength of electronic correlations in a material is calculated by the ratio of the kinetic energies K_{opt}/K_{band}, where K_{opt} is the optical kinetic energy and K_{band} the band kinetic energy [51]. According to Ref. [52], the ratio K_{opt}/K_{band} can be obtained via the ratio of spectral weights SW_{intra}/SW_{tot} from the experimental optical conductivity data. The total spectral weight SW_{tot} was computed by integrating $\sigma_1(\omega)$ at 5 K up to 2700 cm^{-1} (0.334 eV), covering both the Drude term and MIR-band, and subtraction of the phonon mode spectral weight. The intraband contribution SW_{intra} was then determined by subtracting the fitted M-band contribution from SW_{tot}. The ratio of SW_{intra}/SW_{tot} for $Pr_2Ir_2O_7$ at 5 K amounts to approximately 0.26, representing a close low value compared to the value of 0.5 observed for its counterpart $Bi_2Ir_2O_7$ [15] and falling within the typical range for many correlated metals [15,51].

In contrast to the well-understood A, B, B', and C excitations, the enigmatic presence of the M-band in the mid-IR region for the metallic nature of $Pr_2Ir_2O_7$ poses an intriguing puzzle. We described the M-band with a Lorentz oscillator positioned at ~0.121 eV and ~0.128 eV for 300 K and 5 K, respectively, aligning closely with reported values for R-pyrochlore iridates [11]. Previously, the M-band was also observed in the other metallic pyrochlores $Bi_2Ir_2O_7$ and $Pb_2Ir_2O_7$, located at around ~0.2 eV and ~0.4 eV, respectively [15,16]. Notably, these energy values exceed the MIR-band position as observed in $Pr_2Ir_2O_7$. The origin of this mid-IR peak in $Bi_2Ir_2O_7$ was suggested to be related to correlation-induced interband transitions. Within the Ruddlesden-Popper (RP) series, Sr_2IrO_4 serves as an MI and displays a double-peak structure in the $\sigma_1(\omega)$ spectrum around 0.5 and 1 eV [39,41]. These peaks correspond to onsite and intersite transitions between $J_{\mathrm{eff}} = 1/2$ and $J_{\mathrm{eff}} = 3/2$ states. As the system undergoes a transition from the insulating state (Sr_2IrO_4) to nearly insulating ($Sr_3Ir_2O_7$), and finally to the metallic state ($SrIrO_3$) within the RP series, the J_{eff} bands shift to lower energies [41]. Notably, $J_{\mathrm{eff}} = 1/2$ is observed

around 0.2 eV for $SrIrO_3$ [41], still higher in energy than the M-band in our $\sigma_1(\omega)$ spectra. This J_{eff} shift is also observed in pyrochlores transitioning from insulating ($Y_2Ir_2O_7$) to the MIT side ($Sm_2Ir_2O_7$) [11]. In MIT-based $Nd_2Ir_2O_7$, an absorption band is observed, exhibiting a notable shift from approximately 1 eV to around 0.1 eV with lowering the temperature from 290 K to 5 K. Despite this shift, a charge gap of 45 meV remains evident at 5 K and goes to the zero-gap state by Rh doping (x) [12]. Although the expected magnitude of U for $5d$ Ir oxides is below 1 eV [28,39–41], it is noteworthy that the bandwidth of the $J_{\text{eff}} = 1/2$ band, shaped by SOC, may also exhibit narrow characteristics.

Moreover, in the context of the bandwidth during the transition from an MI to a metallic state, it has been observed that a QP peak tends to appear near the Fermi level E_F at low temperatures [44,53,54], situated between the lower and upper Hubbard bands, as illustrated in Fig. 6. As the system undergoes a transition toward a more metallic state, the QP peak is expected to intensify with reductions in the Hubbard bands. Accordingly, one expects several contributions in the optical conductivity spectrum, namely (i) a coherent peak centered at zero energy, (ii) an absorption band due to electronic excitations between the Hubbard bands and the QP peak, and (iii) robust $p - d$ transitions situated at higher energies [53]. Furthermore, within the Hubbard model, it is expected that the spectral density of the QP band increases with lowering the temperature [55].

In our data, we observe the expected spectral features along with a moderate increase in both mode strength S_M of the M-band and SW_D of the Drude term as the temperature decreases. This phenomenon could potentially be attributed to the QP peak feature in the present system, where the transitions take place from the lower Hubbard band to the QP peak or from the QP peak to the upper Hubbard band, as indicated by the green arrows and labeled by M in Fig. 6. We, however, note that the spectral weight transfer from high to low energies [see Fig. 4(b)] cannot be explained within this scenario.

Finally, we note that a mid-IR absorption band is observed in the optical conductivity spectrum of many transition-metal oxides and has been attributed to the excitations of polarons formed due to strong electron-phonon coupling [56–61]. Also for the closely related metallic pyrochlore iridate $Bi_2Ir_2O_7$, the possible relevance of electron-phonon coupling effects has been discussed [15]. Further theoretical investigations are needed to unravel the impact of electronic correlations and electron-phonon coupling on the low-frequency optical response in metallic and semimetallic iridates.

V. CONCLUSIONS

In summary, our investigation of the pyrochlore iridate $Pr_2Ir_2O_7$ has provided insights into its magnetic, lattice dynamical, and electronic properties. Raman spectroscopy confirmed the cubic $Fd\bar{3}m$ crystal symmetry, whereas dc magnetic susceptibility exhibits the PM nature of $Pr_2Ir_2O_7$. Resistivity measurements show its metallic behavior, further supported by optical conductivity analysis. Notably, the optical conductivity spectrum featured a mid-IR absorption band, intensifying at lower temperatures due to spectral weight redistribution, highlighting the role of correlation effects. Furthermore, our optical response analysis suggests that $Pr_2Ir_2O_7$ lies in proximity to a WSM phase.

ACKNOWLEDGMENTS

H.K. acknowledges support provided by the Deutsche Forschungsgemeinschaft (German Research Foundation), Germany, under Grant No. KU 4080/2-1 (495076551). P.T. was supported by the Alexander von Humboldt Foundation. This work was funded by the Deutsche Forschungsgemeinschaft, TRR 360–492547816.

[1] D. Pesin and L. Balents, Mott physics and band topology in materials with strong spin–orbit interaction, Nat. Phys. **6**, 376 (2010).

[2] W. Witczak-Krempa, G. Chen, Y. B. Kim, and L. Balents, Correlated quantum phenomena in the strong spin-orbit regime, Annu. Rev. Condens. Matter Phys. **5**, 57 (2014).

[3] X. Wan, A. M. Turner, A. Vishwanath, and S. Y. Savrasov, Topological semimetal and Fermi-arc surface states in the electronic structure of pyrochlore iridates, Phys. Rev. B **83**, 205101 (2011).

[4] E.-G. Moon, C. Xu, Y. B. Kim, and L. Balents, Non-Fermi-liquid and topological states with strong spin-orbit coupling, Phys. Rev. Lett. **111**, 206401 (2013).

[5] K. Matsuhira, M. Wakeshima, Y. Hinatsu, and S. Takagi, Metal–insulator transitions in pyrochlore oxides $Ln_2Ir_2O_7$, J. Phys. Soc. Jpn. **80**, 094701 (2011).

[6] S. Nakatsuji, Y. Machida, Y. Maeno, T. Tayama, T. Sakakibara, J. V. Duijn, L. Balicas, J. N. Millican, R. T. Macaluso, and J. Y. Chan, Metallic spin-liquid behavior of the geometrically frustrated Kondo lattice $Pr_2Ir_2O_7$, Phys. Rev. Lett. **96**, 087204 (2006).

[7] H. Kumar and A. K. Pramanik, Nonequilibrium low temperature phase in pyrochlore iridate $Y_2Ir_2O_7$: Possibility of glass-like dynamics, J. Magn. Magn. Mater. **409**, 20 (2016).

[8] H. Kumar, K. C. Kharkwal, K. Kumar, K. Asokan, A. Banerjee, and A. K. Pramanik, Magnetic and transport properties of the pyrochlore iridates $(Y_{1-x}Pr_x)_2Ir_2O_7$: Role of f-d exchange interaction and d-p orbital hybridization, Phys. Rev. B **101**, 064405 (2020).

[9] N. Taira, M. Wakeshima, and Y. Hinatsu, Magnetic properties of iridium pyrochlores $R_2Ir_2O_7$ (R = Y, Sm, Eu and Lu), J. Phys.: Condens. Matter **13**, 5527 (2001).

[10] H. Kumar, R. Chaurasia, P. Kumari, and A. K. Pramanik, Structural, magnetic, and electronic transport properties of pyrochlore iridate $Pr_2Ir_2O_7$, AIP Conf. Proc. **1942**, 130058 (2018).

[11] K. Ueda, J. Fujioka, and Y. Tokura, Variation of optical conductivity spectra in the course of bandwidth-controlled metal-insulator transitions in pyrochlore iridates, Phys. Rev. B **93**, 245120 (2016).

[12] K. Ueda, J. Fujioka, Y. Takahashi, T. Suzuki, S. Ishiwata, Y. Taguchi, and Y. Tokura, Variation of charge dynamics in

the course of metal-insulator transition for pyrochlore-type $Nd_2Ir_2O_7$, Phys. Rev. Lett. **109**, 136402 (2012).

[13] K. Wang, B. Xu, C. W. Rischau, N. Bachar, B. Michon, J. Teyssier, Y. Qiu, T. Ohtsuki, B. Cheng, N. P. Armitage, S. Nakatsuji, and D. van der Marel, Unconventional free charge in the correlated semimetal $Nd_2Ir_2O_7$, Nat. Phys. **16**, 1194 (2020).

[14] A. B. Sushkov, J. B. Hofmann, G. S. Jenkins, J. Ishikawa, S. Nakatsuji, S. Das Sarma, and H. D. Drew, Optical evidence for a Weyl semimetal state in pyrochlore $Eu_2Ir_2O_7$, Phys. Rev. B **92**, 241108(R) (2015).

[15] Y. S. Lee, S. J. Moon, S. C. Riggs, M. C. Shapiro, I. R. Fisher, B. W. Fulfer, J. Y. Chan, A. F. Kemper, and D. N. Basov, Infrared study of the electronic structure of the metallic pyrochlore iridate $Bi_2Ir_2O_7$, Phys. Rev. B **87**, 195143 (2013).

[16] Y. Hirata, M. Nakajima, Y. Nomura, H. Tajima, Y. Matsushita, K. Asoh, Y. Kiuchi, A. G. Eguiluz, R. Arita, T. Suemoto, and K. Ohgushi, Mechanism of enhanced optical second-harmonic generation in the conducting pyrochlore-type $Pb_2Ir_2O_{7-x}$ oxide compound, Phys. Rev. Lett. **110**, 187402 (2013).

[17] P. Goswami, B. Roy, and S. Das Sarma, Competing orders and topology in the global phase diagram of pyrochlore iridates, Phys. Rev. B **95**, 085120 (2017).

[18] T. Kondo, M. Nakayama, R. Chen, J. J. Ishikawa, E. G. Moon, T. Yamamoto, Y. Ota, W. Malaeb, H. Kanai, Y. Nakashima, Y. Ishida, R. Yoshida, H. Yamamoto, M. Matsunami, S. Kimura, N. Inami, K. Ono, H. Kumigashira, S. Nakatsuji, L. Balents, and S. Shin, Quadratic Fermi node in a 3D strongly correlated semimetal, Nat. Commun. **6**, 10042 (2015).

[19] Y. Tokiwa, J. J. Ishikawa, S. Nakatsuji, and P. Gegenwart, Quantum criticality in a metallic spin liquid, Nat. Mater. **13**, 356 (2014).

[20] Y. Machida, S. Nakatsuji, Y. Maeno, T. Tayama, T. Sakakibara, and S. Onoda, Unconventional anomalous Hall effect enhanced by a noncoplanar spin texture in the frustrated Kondo lattice $Pr_2Ir_2O_7$, Phys. Rev. Lett. **98**, 057203 (2007).

[21] Y. Machida, S. Nakatsuji, S. Onoda, T. Tayama, and T. Sakakibara, Time-reversal symmetry breaking and spontaneous Hall effect without magnetic dipole order, Nature (London) **463**, 210 (2010).

[22] L. Savary, E.-G. Moon, and L. Balents, New type of quantum criticality in the pyrochlore iridates, Phys. Rev. X **4**, 041027 (2014).

[23] K. Ueda, H. Ishizuka, M. Kriener, S. Kitou, D. Maryenko, M. Kawamura, T.-H. Arima, M. Kawasaki, and Y. Tokura, Experimental signatures of a versatile Weyl semimetal in a pyrochlore iridate with spin-ice-like magnetic orders, Phys. Rev. B **105**, L161102 (2022).

[24] J. N. Millican, R. T. Macaluso, S. Nakatsuji, Y. Machida, Y. Maeno, and J. Y. Chan, Crystal growth and structure of $R_2Ir_2O_7$ (R = Pr, Eu) using molten KF, Mater. Res. Bull. **42**, 928 (2007).

[25] H. Kumar, P. Telang, A. Jesche, and C. A. Kuntscher, Crystal growth of metallic pyrochlore iridate $Pr_2Ir_2O_7$ and its characterization, To be published somewhere else.

[26] A. W. Sleight and A. P. Ramirez, Disappearance of the metal-insulator transition in iridate pyrochlores on approaching the ideal $R_2Ir_2O_7$ stoichiometry, Solid State Commun. **275**, 12 (2018).

[27] M. Köpf, S. H. Lee, H. Kumar, Z. Q. Mao, and C. A. Kuntscher, Infrared study of the layered magnetic insulator $Mn(Bi_{0.07}Sb_{0.93})_2Te_4$ at low temperatures, Phys. Rev. B **105**, 195125 (2022).

[28] H. Kumar, M. Köpf, A. Ullrich, M. Klinger, A. Jesche, and C. A. Kuntscher, Fluorite-related iridate Pr_3IrO_7: Crystal growth, structure, magnetism, thermodynamic, and optical properties, J. Phys.: Condens. Matter **34**, 485806 (2022).

[29] D. B. Tanner, Use of x-ray scattering functions in Kramers-Kronig analysis of reflectance, Phys. Rev. B **91**, 035123 (2015).

[30] A. B. Kuzmenko, Kramers-Kronig constrained variational analysis of optical spectra, Rev. Sci. Instruments **76**, 083108 (2005).

[31] H. Kumar, R. S. Dhaka, and A. K. Pramanik, Evolution of structure, magnetism, and electronic transport in the doped pyrochlore iridate $Y_2Ir_{2-x}Ru_xO_7$, Phys. Rev. B **95**, 054415 (2017).

[32] Y. Machida, S. Nakatsuji, H. Tonomura, T. Tayama, T. Sakakibara, J. Van Duijn, C. Broholm, and Y. Maeno, Crystalline electric field levels and magnetic properties of the metallic pyrochlore compound $Pr_2Ir_2O_7$, J. Phys. Chem. Solids **66**, 1435 (2005).

[33] H. Takatsu, K. Watanabe, K. Goto, and H. Kadowaki, Comparative study of low-temperature x-ray diffraction experiments on $R_2Ir_2O_7$ (R = Nd, Eu, and Pr), Phys. Rev. B **90**, 235110 (2014).

[34] K. Ueda, R. Kaneko, A. Subedi, M. Minola, B. J. Kim, J. Fujioka, Y. Tokura, and B. Keimer, Phonon anomalies in pyrochlore iridates studied by Raman spectroscopy, Phys. Rev. B **100**, 115157 (2019).

[35] H. Kumar, V. G. Sathe, and A. K. Pramanik, Spin–phonon and electron–phonon coupling in pyrochlore iridates $(Y_{1-x}Pr_x)_2Ir_2O_7$: An investigation with Raman spectroscopy, J. Phys. Chem. C **127**, 13178 (2023).

[36] M. Rosalin, P. Telang, S. Singh, D. V. S. Muthu, and A. K. Sood, Non-Fermi-liquid signatures of quadratic band touching and phonon anomalies in metallic $Pr_2Ir_2O_7$, Phys. Rev. B **108**, 195144 (2023).

[37] J. Son, B. C. Park, C. H. Kim, H. Cho, S. Y. Kim, L. J. Sandilands, C. Sohn, J. G. Park, S. J. Moon, and T. W. Noh, Unconventional spin-phonon coupling via the Dzyaloshinskii–Moriya interaction, npj Quantum Mater. **4**, 17 (2019).

[38] M. Dressel and G. Grüner, *Electrodynamics of Solids: Optical Properties of Electrons in Matter* (Cambridge University Press, Cambridge, 2002).

[39] B. J. Kim, H. Jin, S. J. Moon, J. Y. Kim, B. G. Park, C. S. Leem, J. Yu, T. W. Noh, C. Kim, S. J. Oh, J. H. Park, V. Durairaj, G. Cao, and E. Rotenberg, Novel $J_{\rm eff} = 1/2$ Mott state induced by relativistic spin-orbit coupling in Sr_2IrO_4, Phys. Rev. Lett. **101**, 076402 (2008).

[40] V. Hermann, J. Ebad-Allah, F. Freund, I. M. Pietsch, A. Jesche, A. A. Tsirlin, J. Deisenhofer, M. Hanfland, P. Gegenwart, and C. A. Kuntscher, High-pressure versus isoelectronic doping effect on the honeycomb iridate Na_2IrO_3, Phys. Rev. B **96**, 195137 (2017).

[41] S. J. Moon, H. Jin, K. W. Kim, W. S. Choi, Y. S. Lee, J. Yu, G. Cao, A. Sumi, H. Funakubo, C. Bernhard, and T. W. Noh, Dimensionality-controlled insulator-metal transition and correlated metallic state in 5*d* transition metal oxides $Sr_{n+1}Ir_nO_{3n+1}$ (n = 1, 2, and ∞), Phys. Rev. Lett. **101**, 226402 (2008).

[42] V. Hermann, J. Ebad-Allah, F. Freund, A. Jesche, A. A. Tsirlin, P. Gegenwart, and C. A. Kuntscher, Optical signature of the

pressure-induced dimerization in the honeycomb iridate α – Li_2IrO_3, Phys. Rev. B **99**, 235116 (2019).

[43] T. Ohtsuki, Z. Tian, A. Endo, M. Halim, S. Katsumoto, Y. Kohama, K. Kindo, M. Lippmaa, and S. Nakatsuji, Strain-induced spontaneous Hall effect in an epitaxial thin film of a Luttinger semimetal, Proc. Natl. Acad. Sci. USA **116**, 8803 (2019).

[44] I. Kézsmárki, N. Hanasaki, D. Hashimoto, S. Iguchi, Y. Taguchi, S. Miyasaka, and Y. Tokura, Charge dynamics near the electron-correlation induced metal-insulator transition in pyrochlore-type molybdates, Phys. Rev. Lett. **93**, 266401 (2004).

[45] Á. Bácsi and A. Virosztek, Low-frequency optical conductivity in graphene and in other scale-invariant two-band systems, Phys. Rev. B **87**, 125425 (2013).

[46] M. B. Schilling, Optical studies on Dirac and Weyl semimetals, Ph.D. thesis, University of Stuttgart, Germany, 2018.

[47] P. Hosur, S. A. Parameswaran, and A. Vishwanath, Charge transport in Weyl semimetals, Phys. Rev. Lett. **108**, 046602 (2012).

[48] M. Corasaniti, R. Yang, Z. Hu, M. Abeykoon, C. Petrovic, and L. Degiorgi, Evidence for correlation effects in noncentrosymmetric type-II Weyl semimetals, Phys. Rev. B **104**, L121112 (2021).

[49] I. Kapon, C. W. Rischau, B. Michon, K. Wang, B. Xu, Q. Yang, S. Nakatsuji, and D. van der Marel, Magnetic field tuning of valley population in the Weyl phase of $Nd_2Ir_2O_7$, Phys. Rev. Res. **4**, 023056 (2022).

[50] B. Cheng, T. Ohtsuki, D. Chaudhuri, S. Nakatsuji, M. Lippmaa, and N. P. Armitage, Dielectric anomalies and interactions in the three-dimensional quadratic band touching Luttinger semimetal $Pr_2Ir_2O_7$, Nat. Commun. **8**, 2097 (2017).

[51] D. N. Basov, R. D. Averitt, D. van der Marel, M. Dressel, and K. Haule, Electrodynamics of correlated electron materials, Rev. Mod. Phys. **83**, 471 (2011).

[52] L. Degiorgi, Electronic correlations in iron-pnictide superconductors and beyond: Lessons learned from optics, New J. Phys. **13**, 023011 (2011).

[53] J. S. Lee, S. J. Moon, T. W. Noh, T. Takeda, R. Kanno, S. Yoshii, and M. Sato, Optical investigations on $Y_{2-x}Bi_xRu_2O_7$: Electronic structure evolutions related to the metal-insulator transition, Phys. Rev. B **72**, 035124 (2005).

[54] J. S. Lee, Y. S. Lee, T. W. Noh, K. Char, J. Park, S.-J. Oh, J.-H. Park, C. B. Eom, T. Takeda, and R. Kanno, Optical investigation of the electronic structures of $Y_2Ru_2O_7$, $CaRuO_3$, $SrRuO_3$, and $Bi_2Ru_2O_7$, Phys. Rev. B **64**, 245107 (2001).

[55] J. Merino and R. H. McKenzie, Transport properties of strongly correlated metals: A dynamical mean-field approach, Phys. Rev. B **61**, 7996 (2000).

[56] S. Lupi, P. Maselli, M. Capizzi, P. Calvani, P. Giura, and P. Roy, Evolution of a polaron band through the phase diagram of $Nd_{2-x}Ce_xCuO_{4-y}$, Phys. Rev. Lett. **83**, 4852 (1999).

[57] X.-X. Bi and P. C. Eklund, Polaron contribution to the infrared optical response of $La_{2-x}Sr_xCuO_{4+\delta}$ and $La_{2-x}Sr_xNiO_{4+\delta}$, Phys. Rev. Lett. **70**, 2625 (1993).

[58] C. A. Kuntscher, D. van der Marel, M. Dressel, F. Lichtenberg, and J. Mannhart, Signatures of polaronic excitations in quasi-one-dimensional $LaTiO_{3.41}$, Phys. Rev. B **67**, 035105 (2003).

[59] J. Ebad-Allah, L. Baldassarre, M. Sing, R. Claessen, V. A. M. Brabers, and C. A. Kuntscher, Polaron physics and crossover transition in magnetite probed by pressure-dependent infrared spectroscopy, J. Phys.: Condens. Matter **25**, 035602 (2013).

[60] J. T. Devreese, S. N. Klimin, J. L. M. van Mechelen, and D. van der Marel, Many-body large polaron optical conductivity in $SrTi_{1-x}Nb_xO_3$, Phys. Rev. B **81**, 125119 (2010).

[61] M. Reticcioli, U. Diebold, G. Kresse, and C. Franchini, Small polarons in transition metal oxides, in *Handbook of Materials Modeling*, edited by W. Andreoni and S. Yip (Springer, Cham, 2018), pp. 1–39.